

# Intrinsic defects and 4d/5d transition metal defects in Cr<sub>2</sub>O<sub>3</sub>: pathways to enhance the Néel temperature

Xuecong Wang<sup>1</sup> and Sai Mu<sup>1</sup>

<sup>1</sup>*Department of Physics and Astronomy and SmartState Center for Experimental Nanoscale Physics,  
University of South Carolina, Columbia, South Carolina, 29208, USA*

First-principles calculations are employed to explore avenues to increase the Néel temperature ( $T_N$ ) of the magnetoelectric antiferromagnet Cr<sub>2</sub>O<sub>3</sub> through doping. Employing the hybrid functional method, we calculate the formation energy of intrinsic defects and transition metal dopants (Mo, W, Nb, Ta, Zr, and Hf) to assess their likelihood of formation. Intrinsic defect calculations indicate that Cr interstitials and oxygen vacancies dominate under Cr-rich conditions, whereas Cr vacancies prevail under O-rich conditions. Notably, under Cr-rich conditions, the Fermi level can be pinned slightly above mid-gap due to the formation of Cr interstitials and oxygen vacancies. To assess the influence of dopant on  $T_N$  of Cr<sub>2</sub>O<sub>3</sub>, we calculate the enhancement of the exchange energy for the spin on the dopant site or on adjacent Cr site using the supercell method. Our study identifies isovalent Mo and W substitution on Cr site as the most promising candidates to increase Néel temperature due to the impurity-mediated enhanced exchange interaction for half-filled bands. Formation energy calculations indicate that Mo and W substitution on Cr are easier to form under Cr-rich conditions and a Fermi level near or slightly above the midgap renders a desirable *neutral* Mo and W defect. This is assisted by the formation of intrinsic Cr interstitial and O vacancy under Cr-rich conditions. These findings offer a route to utilize defects for higher  $T_N$  and enhanced performance of Cr<sub>2</sub>O<sub>3</sub> in magnetoelectric devices and furnish invaluable insights for directing subsequent experimental endeavors.

## I. INTRODUCTION

Magnetoelectric antiferromagnets [1] have garnered considerable attention due to their applications in magnetoelectronic devices that leverage the electric control of magnetization [2–4]. Among these materials, Cr<sub>2</sub>O<sub>3</sub> serves as the active magnetoelectric material in voltage-controlled exchange bias devices, which are promising for magnetic memory and logic applications because of their nonvolatility and low power consumption.[5]

While Cr<sub>2</sub>O<sub>3</sub> exhibits the highest Néel temperature ( $T_N = 307K$ ) among magnetoelectric antiferromagnets [6], its  $T_N$  in room temperature region is still not high enough for practical applications. This calls for acute investigations to increase  $T_N$  of Cr<sub>2</sub>O<sub>3</sub>. Two prominent approaches have been explored to achieve higher  $T_N$ : mechanical strain[7, 8] and chemical doping [9, 10]. In this study, we concentrate on the doping approach. Previous first-principles study suggested that substitutional boron doping on the oxygen site could effectively raise the  $T_N$  of Cr<sub>2</sub>O<sub>3</sub> through impurity-mediated superexchange-like interactions [9], a finding demonstrated experimentally later [10, 11]. As opposed to the anion impurity, cation impurities have been less successful in achieving high  $T_N$  of Cr<sub>2</sub>O<sub>3</sub>. Incorporation of 3d transition metal dopants (Ti, V, Mn, Fe, Co, Ni) [9] and *isovalent* 4d transition metal dopants (Zr, Nb, Mo) [12] on the cation Cr site has been investigated for a higher  $T_N$ . However, *only* Mo exhibits some potential for a higher  $T_N$  [12], while the rest candidates have proven detrimental to  $T_N$  enhancement.

Previous calculations on enhancing the  $T_N$  of Cr<sub>2</sub>O<sub>3</sub> has focused exclusively on the substitutional configuration of dopant, neglecting the potential defect in-

corporation on interstitial sites. Additionally, the likelihood of incorporation of these defects remains unexplored. Furthermore, previous first-principles studies have only considered isovalent defects, overlooking other possible charge states of the dopant and their impact on  $T_N$ . Consequently, it is crucial and urgent to perform the defect formation energy calculations to evaluate the likelihood of defect incorporation, determine the feasible charge states of the defect, and assess their influence on the  $T_N$ .

Intrinsic defects determine the electrical properties of Cr<sub>2</sub>O<sub>3</sub>, with the predominant ones significantly influencing the position of Fermi level and consequently the charge state of extrinsic defects. Moreover, the spin states of these intrinsic defects might affect its formation energy and the magnetism of Cr<sub>2</sub>O<sub>3</sub>. Although the formation energies of some of the intrinsic defects have been explored previously [13–15], the accuracy of previous results is limited by the methodology to take into account self-interaction and the spin states of intrinsic defects have not been addressed clearly in these studies.

Using density functional theory calculations, we conduct a comprehensive investigation of formation energies of both intrinsic defects and selected 4d and 5d transition metal foreign defects. The likelihood of defect formation on the cation site and interstitial site and its charge states are addressed from hybrid functional calculations. The influence of the defects on the  $T_N$  of Cr<sub>2</sub>O<sub>3</sub> is explored and we found neutral Mo and W are most promising to raise the  $T_N$  and Cr-rich conditions will facilitate its formation. A rough estimate gives that 1 % Mo (W) doping increase the  $T_N$  by 5.8 % (8.9 %). Intrinsic defect calculations further demonstrated that the neutral charge state of Mo could be realized under Cr-rich conditions,

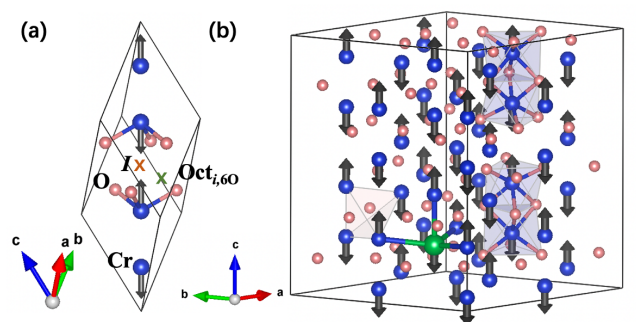


FIG. 1. (Color online) (a) Rhombohedral primitive cell of Cr<sub>2</sub>O<sub>3</sub>. Larger blue and pink spheres represent Cr atoms with opposite spin moments; smaller red spheres display the O atoms. (b)  $2 \times 2 \times 1$  hexagonal supercell with doped Mo atom (green sphere). The bonds connect Mo defect with the nearest Cr neighbour and three second nearest Cr neighbor.

through the Fermi level pinning by the predominant Cr interstitial and O vacancy.

## II. METHODOLOGY

### A. Computational details

Our first-principles calculations were performed using the Vienna Ab initio Simulation Package (VASP 6.3.2) [16, 17]. Projector augmented wave potentials [18] were used and the exchange-correlation was treated within generalized gradient approximation (GGA) [19]. The valence electron wavefunctions were expanded with a kinetic energy cutoff of 520 eV and the valence electron configurations are  $3d^5 4s^1$  for Cr and  $2s^2 2p^4$  for O. We simulated bulk Cr<sub>2</sub>O<sub>3</sub> using the 10-atom rhombohedral primitive cell [see Fig. 1 (a)]. Four Cr atoms contain two different sublattices with opposite spins, forming  $+ - + -$  G-type antiferromagnetic spin ordering. Gaussian smearing of 0.1 eV (0.02 eV) and a  $\Gamma$ -centered  $3 \times 3 \times 3$  ( $5 \times 5 \times 5$ ) Monkhorst-Pack  $k$ -point mesh [20] were used for the structural relaxation [density of states (DOS) calculation].

To take into account of the Coulomb correlation of the localized  $d$  orbitals on Cr or on transition metal defects, we employed the hybrid functional of Heyd, Scuseria, and Ernzerhof (HSE) [21] with a mixing parameter  $\alpha = 0.20$  and a screening parameter of 0.3. The combination of these parameters yields a band gap of 3.45 eV, which agrees well with the experimental value (3.4 eV) [22–24]. The dependence of the band gap and lattice parameters on the mixing parameter and screening parameter were investigated and the optimal combination of parameters is selected accordingly. [See more details in supplementary materials (SM)]

Defects were simulated using the supercell approach [25, 26]. Six  $4d/5d$  transition metal defects are considered: Mo ( $4d^5 5s^1$ ), W ( $5d^4 6s^2$ ), Nb ( $4d^4 5s^1$ ), Ta

( $5d^3 6s^2$ ), Zr ( $4d^2 5s^2$ ), and Hf ( $5d^2 6s^2$ ). A  $2 \times 2 \times 1$  hexagonal Cr<sub>2</sub>O<sub>3</sub> supercell with 120 atoms [see Fig. 1(b)] was built to host a single defect, and a  $\Gamma$  point was used for Brillouin zone integration [27]. The magnetic ground state of bulk Cr<sub>2</sub>O<sub>3</sub> is G-type antiferromagnetic. With the inclusion of the transition metal defects, the spin ordering of the bulk is typically preserved. However, multiple spin states – such as high-spin and low-spin configurations – can emerge at the defect site, depending on the competition between the crystal field splitting and the on-site exchange. To identify the most favorable spin state, we initialized the defect site with various local moments. The initial atomic positions of the defective supercell were randomly shifted and then relaxation was carried out until the Hellmann-Feynman force on all atoms were reduced below 0.01 eV/Å.

### B. Exchange energy

To evaluate the influence of impurities on the Néel temperature of Cr<sub>2</sub>O<sub>3</sub>, we compute the exchange energy (hereafter denoted as  $E_{\text{ex}}$ ), which represents the energy cost to invert the spin on a magnetic atom. [9] This energy is directly associated with the strength of the exchange interaction between the central spin and its neighboring spins. For supercell calculations with impurity, we calculate the exchange energies on the cation impurity and nearby Cr atoms. Four neighboring Cr atoms are considered for the exchange energy calculation: one nearest Cr neighbor along the (0001) direction, and three next-to-nearest Cr neighbors in the buckled plane. [see Fig. 1(b)] From our HSE calculations, the exchange energy for bulk Cr<sub>2</sub>O<sub>3</sub> is 178 meV. If we find this value is averagely enhanced after doping, we expect an increase of the exchange interaction and the Néel temperature.

In classical mean field theory, the Néel temperature is proportional to the exchange energy as:

$$T_N = \frac{E_{\text{ex}}}{6k_B} \quad (1)$$

where  $T_N$  represents the Néel temperature,  $E_{\text{ex}}$  denotes the exchange energy, and  $k_B$  is the Boltzmann constant. Hence, we can estimate the change in the Néel temperature by comparing the average  $E_{\text{ex}}$  of the defective supercell to that of the bulk. The average  $E_{\text{ex}}$  is obtained by averaging  $E_{\text{ex}}$  on all magnetic ions in the defective supercell.

### C. Defect formation energy

The stability of defects is assessed by calculating their formation energies ( $E^f$ ). The formation energy of a single cation substitutional defect  $X$  in charge state  $q$  is

given by [25]:

$$E^f[X^q] = E_{\text{tot}}[X^q] - E_{\text{tot}}[\text{bulk}] - \mu_X + \mu_{\text{Cr}} + qE_F + \Delta^q. \quad (2)$$

Here,  $E_{\text{tot}}[\text{bulk}]$  and  $E_{\text{tot}}[X^q]$  represent the total energies of a bulk supercell and a supercell with the defect, respectively. Chemical potential for element  $i$  is denoted as  $\mu_i$ . The Fermi level, or the electron's chemical potential, is denoted by  $E_F$  and is referenced to the valence-band maximum (VBM). The term  $\Delta^q$  is a finite-size correction for the electrostatic interaction between charged defect and its images [28, 29]. This correction is calculated using an HSE dielectric tensor ( $\epsilon^{\parallel} = 13.0$ ,  $\epsilon^{\perp} = 11.8$ ), which aligns closely with the experimental dielectric constant [30].

The chemical potential of an atomic species, denoted as  $\mu_i$ , signifies the energy cost of atom exchange with a reservoir. It is given by  $\mu_i = \mu_{\text{ref},i} + \Delta\mu_i$ , where  $\mu_{\text{ref},i}$  is the reference chemical potential of species  $i$ , and  $\Delta\mu_i$  represents the atomic species' environmental abundance [25]. For Cr and O, the references are the energy of bulk Cr metal and the  $\text{O}_2$  molecule, respectively. In thermodynamic equilibrium,  $\Delta\mu_i$  satisfies:

$$2 \times \Delta\mu_{\text{Cr}} + 3 \times \Delta\mu_{\text{O}} = \Delta H_f(\text{Cr}_2\text{O}_3) \quad (3)$$

Here,  $\Delta H_f(\text{Cr}_2\text{O}_3)$  is the formation enthalpy of  $\text{Cr}_2\text{O}_3$ . Our calculated  $\Delta H_f(\text{Cr}_2\text{O}_3)$  is 10.82 eV, aligning well with the experimental value of 11.69 eV [31]. To prevent the formation of elemental phases,  $\Delta\mu_i \leq 0$ . Under the Cr-rich conditions,  $\Delta\mu_{\text{Cr}} = 0$ , yielding  $\Delta\mu_{\text{O}} = \frac{1}{3}\Delta H_f(\text{Cr}_2\text{O}_3)$ . While under the O-rich conditions,  $\Delta\mu_{\text{O}} = 0$ , giving  $\Delta\mu_{\text{Cr}} = \frac{1}{2}\Delta H_f(\text{Cr}_2\text{O}_3)$ . Chemical potentials of impurities are determined by their solubility-limiting phases, which are  $\text{MoO}_3$  for Mo,  $\text{Cr}_2\text{WO}_6$  for W,  $\text{TaCrO}_4$  and  $\text{Ta}_2\text{CrO}_6$  for Ta,  $\text{NbCrO}_4$  for Nb,  $\text{ZrO}_2$  for Zr, and  $\text{HfO}_2$  for Hf. Under O-rich conditions, the limiting phases for Mo, W, Nb, Ta, Zr, and Hf are  $\text{Cr}_2\text{Mo}_3\text{O}_{12}$ ,  $\text{Cr}_2\text{WO}_6$ ,  $\text{NbCrO}_4$ ,  $\text{TaCrO}_4$ ,  $\text{ZrO}_2$ , and  $\text{HfO}_2$  respectively. As for the Cr-rich conditions, the limiting phases are bulk metallic Mo, bulk metallic W,  $\text{NbCrO}_4$ ,  $\text{TaCrO}_4$ ,  $\text{ZrO}_2$ , and  $\text{HfO}_2$ , respectively.

Defect charge-state transition levels  $\varepsilon(q/q')$  are defined as the Fermi-level position where the most stable charge state changes from  $q$  to  $q'$ . They are calculated as

$$\varepsilon(q/q') = \frac{E^f[X^q; E_F = 0] - E^f[X^{q'}; E_F = 0]}{q' - q} \quad (4)$$

where  $E^f[X^q; E_F = 0]$  is the formation energy of defect  $X$  with charge  $q$  when the Fermi level is at the VBM.

The binding energy of defect complex is also calculated to explore the stability of the complex once it is formed. Take  $(\text{Cr}_i - V_{\text{Cr}})^n$  in charge state  $n$  for example, the binding energy is defined in terms of formation energies,

$$E_{\text{bind}}[(\text{Cr}_i - V_{\text{Cr}})^n] = E^f(\text{Cr}_i^m) + E^f(V_{\text{Cr}}^{n-m}) - E^f[(\text{Cr}_i - V_{\text{Cr}})^n], \quad (5)$$

where  $n$ ,  $m$  and  $n - m$  denotes charge states of the complex,  $\text{Cr}_i$  and  $V_{\text{Cr}}$ . Different  $m$  are tested and the one with the lowest binding energy is adopted. Charge neutrality relation is kept to evaluate the binding energy. By definition, a positive binding energy indicates a stable, bound defect complex.

#### D. Nudged elastic band calculation

Migration barriers of Cr vacancy are calculated using the climbing-image nudged elastic band (cNEB) method [32]. The initial and final structure correspond to a vacancy forming on two Cr sublattices that are inversion symmetry connected respectively. They are energetically degenerate but the net magnetizations of them are opposite. We divide the NEB paths into two segments, separated by an intermediate state of a split vacancy (denoted as  $V_{\text{Cr}}^s$ ). The split vacancy position depicts one Cr occupying the inversion center while two normal vacancies forming on its nearby Cr neighbors along the  $c$  axis. Due to the dual choice of Cr spins near the inversion center, two intermediate states with either spin choice are selected such that each segment of the NEB path is spin conserved. The atomic positions of two intermediate states are close, and we use configurational diagram to connect the two intermediate states.

### III. RESULTS AND DISCUSSIONS

#### A. $\text{Cr}_2\text{O}_3$ bulk properties

As mentioned in Sec. II A, the mixing parameter of 0.2 and screening parameter of 0.3 are chosen throughout DFT calculations, yielding agreements with the measured bandgap, local moment on Cr and lattice parameters in bulk  $\text{Cr}_2\text{O}_3$ . Comparison of the lattice parameters, band gaps, atomic positions between experiment and theory is shown in Table I. More details about the mixing parameter dependent bulk properties can be found in Sec. S1 of SM.

Figure 2 shows the calculated total and partial density of states (DOS) of  $\text{Cr}_2\text{O}_3$  using HSE, which agree well with previous works [33]. Due to the quasi-octahedral crystal field, Cr  $3d$  orbitals are split into lower-lying  $t_{2g}$  states and higher-lying  $e_g$  states, which are labeled in Fig. 2.  $t_{2g}$  orbitals are half-filled, which favors anti-ferromagnetic spin coupling for direct exchange interactions. [33] Band structure of  $\text{Cr}_2\text{O}_3$  is illustrated in SM. An indirect band gap of 3.42 eV is found from calculation, which compares well with the measured the indirect band gap of 3.40 eV [22, 34].

TABLE I. Lattice parameters (given in Å), local moment ( $\mu$ , given in  $\mu_B$ ) and bandgap of  $\text{Cr}_2\text{O}_3$  ( $E_g$ , given in eV). Previous calculation and experiment results are compared. Wyckoff positions for atoms in hexagonal  $\text{Cr}_2\text{O}_3$  are also given.

			This work	Expt
$a$ (Å)			4.9668	4.9507 <sup>a</sup>
$c$ (Å)			13.6472	13.5656 <sup>a</sup>
$\mu$ ( $\mu_B$ )			2.86	2.48 <sup>b</sup>
$E_g$ (eV)			3.42	3.40 <sup>c</sup>
Site	Position	$x$	$y$	$z$
Cr	12c	0.0000	0.0000	0.6528
O	18e	0.3055	0.0000	0.2500

<sup>a</sup>Reference[35]; <sup>b</sup>Reference[36];

<sup>c</sup>Reference[22–24]

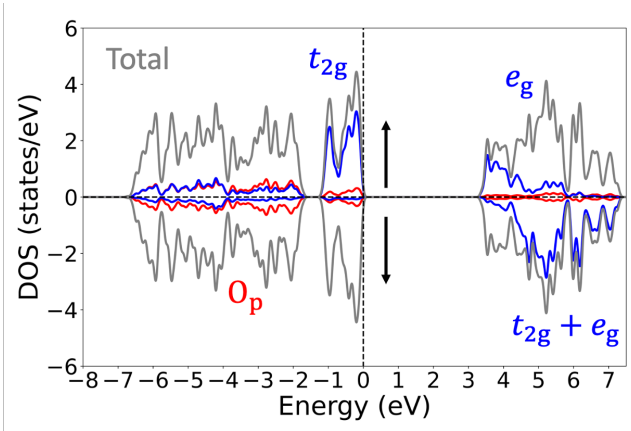


FIG. 2. Density of states per formula unit (f.u.) of  $\text{Cr}_2\text{O}_3$  bulk (grey lines) and partial density of states of  $3d$  orbitals for one Cr with spin up local moment (blue lines) and O- $p$  orbitals (red lines). DOS in majority- and minority-spin channels are plotted as positive and negative, respectively.

## B. Formation of intrinsic defects and complexes

We start from the investigation of the formation of intrinsic defects and their complexes in  $\text{Cr}_2\text{O}_3$ . The following intrinsic defects are considered: O vacancy ( $V_O$ ), O interstitial ( $O_i$ ), O substitution on Cr site ( $O_{Cr}$ ), Cr vacancy ( $V_{Cr}$ ), Cr interstitial ( $Cr_i$ ), Cr substitution on O site ( $Cr_O$ ),  $Cr_i - V_O$  and  $Cr_i - V_{Cr}$ . Note that we were unable to converge the residual force for  $Cr_O$ , so it is not included in this study. Their formation energies under Cr-rich and O-rich conditions are shown in Fig. 3.

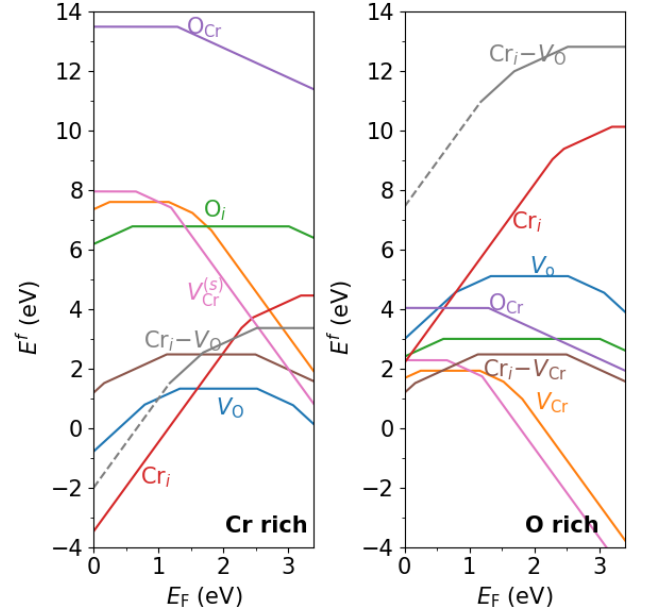


FIG. 3. Formation energy  $E^f$  of intrinsic defects in  $\text{Cr}_2\text{O}_3$  as a function of Fermi level  $E_F$  under (a) Cr-rich and (b) O-rich conditions.

### 1. Intrinsic defects

*a. Cr interstitial* There are two possible sites for cation interstitial: one octahedral site at the inversion center with six surrounding oxygen atoms (see Fig. 1), and the other tetrahedral site with four oxygen vertices (see Fig. S3 in the SM). Energy wise, we found that Cr interstitial ( $Cr_i$ ) strongly prefers the octahedral site at the inversion center and this is also true for all studied interstitial cation impurities. Therefore, we ignore the tetrahedral site when talking about the cation interstitial hereafter.

The formation energy of interstitial chromium ( $Cr_i$ ) under both O-rich and Cr-rich conditions is shown in Fig. 3. Once incorporated,  $Cr_i$  in  $\text{Cr}_2\text{O}_3$  acts as a dominant donor when the Fermi level lies deep within the band gap. The  $(3+/2+)$ ,  $(2+/+)$ , and  $(+/0)$  charge-state transition levels are located 1.12, 0.94, and 0.20 eV below CBM, respectively. It is worth noting that while our calculated  $(2+/+)$  and  $(+/0)$  levels agree well with those reported in Ref. 14, our  $(3+/2+)$  level is 0.64 eV higher. This discrepancy likely arises from differences in the computational methods: our calculations employ a hybrid functional, whereas Ref. 14 used GGA+ $U$ . When the Fermi level is near midgap,  $Cr_i$  favors the  $3+$  charge state.  $Cr_i$  is more readily incorporated under Cr-rich conditions due to its lower formation energy, which is 1.63 eV when the Fermi level is at midgap. As a result,  $Cr_i$  is expected to be the dominant defect in  $\text{Cr}_2\text{O}_3$  under Cr-rich growth conditions, pushing the Fermi level toward the upper part of the band gap due to its donor



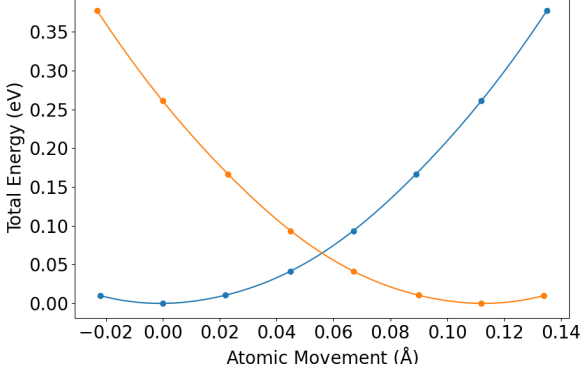


FIG. 4. Blue (orange) dot are calculated data for interstitial Cr atom in spindown (spinup) state. Blue (orange) line are interpolated curve

character.

It is worth noting that the  $\text{Cr}_i^{3+}$  carries a local moment of  $2.73 \mu_B$ . The presence of a magnetic cation at the inversion center breaks the combined inversion–time-reversal symmetry ( $I \otimes T$ ), where  $I$  and  $T$  denote inversion and time-reversal symmetry, respectively. The symmetry breaking induces a local structural relaxation involving  $\text{Cr}_i$  and its six neighboring oxygen atoms.  $\text{Cr}_i$  is slightly displaced from the inversion center, while the surrounding O atoms shift inward toward the interstitial site. As a result, the  $\text{Cr}_i\text{-O}$  bond lengths within the  $\text{Cr}_i\text{O}_6$  octahedron are reduced to  $1.99 \text{ \AA}$  and  $1.97 \text{ \AA}$ , compared to the ideal bond length of  $2.07 \text{ \AA}$  in the absence of symmetry breaking.

Despite the presence of a finite local moment on  $\text{Cr}_i$ , the exchange field at the inversion center is exactly zero by symmetry. This implies the existence of two degenerate  $\text{Cr}_i$  configurations near the inversion center with opposite spin orientations. As expected, we identify both spin-reversed configurations, which are symmetry-equivalent. To evaluate the transition barrier between them, we computed the configurational coordinate diagram (see Fig. 4) and found a small migration barrier of  $62 \text{ meV}$ .

*b. Cr vacancy*  $V_{\text{Cr}}$  is a deep acceptor in  $\text{Cr}_2\text{O}_3$  (see orange line in Fig. 3). The charge-state transition levels  $(+/0)$ ,  $(0/-)$ ,  $(-/2-)$ ,  $(2-/3-)$  of  $V_{\text{Cr}}$  locate at  $0.25$ ,  $1.16$ ,  $1.52$  and  $1.82 \text{ eV}$  above the VBM, respectively. When the Fermi level locates deep in the gap,  $V_{\text{Cr}}$  could be in  $1-$ ,  $2-$  and  $3-$  charge state, acting as an acceptor. For all three negative charge states, the six O atoms around the vacancy relax outward by approximately  $0.12 - 0.14 \text{ \AA}$ . Interestingly, we find that the conventional Cr vacancy ( $V_{\text{Cr}}$ ) is only metastable. A more stable configuration emerges when a nearby Cr (fifth nearest Cr neighbor to  $V_{\text{Cr}}$ ) undergoes a significant relaxation, migrating along the hexagonal axis to an interstitial site (the inversion center, see Fig. 1) in between, thereby forming a dumbbell structure along the hexagonal axis. Here we

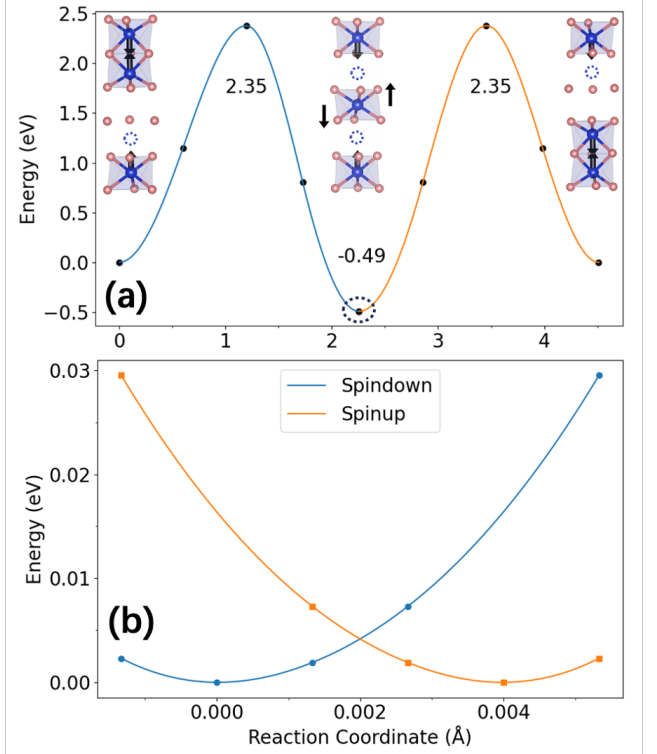


FIG. 5. (a) Migration barrier of  $V_{\text{Cr}}^{3-}$  from a normal Cr vacancy to a split vacancy, and to another normal Cr vacancy with an opposite local moment. (b) Configurational diagram of  $V_{\text{Cr}}^{(s)3-}$  between the spin-up and spin-down intermediate states.

denote this Cr vacancy as split vacancy, i.e.  $V_{\text{Cr}}^{(s)}$ , which is equivalent to a formation of an interstitial Cr together with two Cr vacancies. The creation of the split vacancy is illustrated in Fig. 5.

As shown in Fig. 3, only the  $(0/-)$  and  $(-/3-)$  charge-state transition levels of  $V_{\text{Cr}}^{(s)}$  appear, located at  $0.66 \text{ eV}$  and  $1.22 \text{ eV}$  above the VBM, respectively. When the Fermi level lies deep within the band gap,  $V_{\text{Cr}}^{(s)}$  adopts the  $3-$  charge state. Formation of the  $V_{\text{Cr}}^{(s)3-}$  configuration lowers the formation energy by  $1.10 \text{ eV}$  compared to the ordinary  $V_{\text{Cr}}^{3-}$ . However, realizing  $V_{\text{Cr}}^{(s)3-}$  requires the migration of a nearby Cr atom to an interstitial site—an event that does not occur spontaneously due to a migration barrier. We find this barrier to be approximately  $2.35 \text{ eV}$  [see Fig. 5(a)], indicating that the transition can be activated at high temperatures, allowing both vacancy configurations to form. From NEB calculations which based on total energies of the supercell, the  $V_{\text{Cr}}^{(s)3-}$  is more stable than  $V_{\text{Cr}}^{3-}$  by  $0.49 \text{ eV}$ . We note that this is different from the  $1.10 \text{ eV}$  difference in their formation energies (see Fig. 3). We find that the divergency stems from the charge correction which is included in formation energy calculations but ignored in NEB. Interestingly, the local charge distribution in  $V_{\text{Cr}}^{3-}$  is around this normal

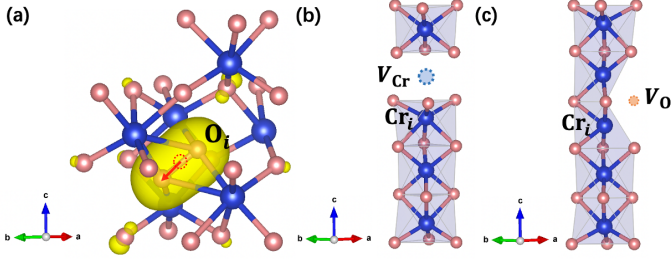


FIG. 6. (a) Local atomic environment around the *neutral*  $O_i^0$ , featured by an interstitial O atom pushing a nearby O away from its ideal lattice site (dashed circle), forming a O–O dumbbell. The isosurface of charge density of  $O_i^0$  is shown in yellow, and the isosurface level is  $0.1 \text{ e}/\text{\AA}^3$ . (b)  $Cr_i - V_{Cr}$  complex with the Cr vacancy shown in black circle. (c)  $Cr_i - V_O$  complex with the O vacancy shown in red circle.

vacancy, while for  $V_{Cr}^{(s)3-}$ , the charges tend to distribute closer to the two vacancy sites within this split vacancy.

We also find that the localized charges associated with the triply charged Cr vacancies ( $V_{Cr}^{3-}$  and  $V_{Cr}^{(s)3-}$ ) are spin-polarized, with a net magnetization of  $3 \mu_B$  for the whole supercell. Similar to  $Cr_i^{3+}$ , the interstitial Cr site within in  $V_{Cr}^{(s)3-}$  also carries a local moment of  $2.7 \mu_B$ . Given that it occupies the inversion center with a minimal exchange field, its local moment could be easily flipped, together with a flipped total magnetization and a tiny local relaxation. Figure 5 (b) shows the calculated the energy profile of both spin-up and spin-down states, as a function of reaction coordinate. The energy barrier to flip the local moment on the interstitial site of  $V_{Cr}^{(s)3-}$  is 72 meV, comparable to the energy barrier (62 meV) for a spin flip in  $Cr_i^{3+}$ . The local spin flipped  $V_{Cr}^{(s)3-}$  can further migrate along  $c$  axis, converting to a normal Cr vacancy with an opposite spin. [see the other segment and structural illustration in Fig. 5(a)]

Additionally, an in-plane split-vacancy configuration was also obtained, in which a vacancy forms at a Cr site located in the same plane as the inversion center, while the Cr atom related by inversion symmetry migrates to the center to form a dumbbell. The structure of this configuration is shown in Fig. S5 of the SM. However, its energy is at least 3.4 eV higher than that of the most stable split-vacancy configuration discussed earlier, and thus it can be safely excluded from further consideration.

In contrast to Cr interstitial, the formation energies of both split Cr vacancy ( $V_{Cr}^{(s)}$ ) and normal chromium vacancy ( $V_{Cr}$ ) are low under extremely O-rich conditions but increases significantly under Cr-rich conditions. Under practical experimental synthesis conditions which are typically intermediate between the Cr-rich and O-rich limits, Cr vacancies can appear in negatively charged states (3–, 2– for  $V_{Cr}$  and 3– for  $V_{Cr}^{(s)}$ ) in insulating samples and act as dominant compensators. Given their moderate formation energies, both  $V_{Cr}$  and  $V_{Cr}^{(s)}$  are ther-

modynamically accessible.

Due to their acceptor nature and low formation energy under O-rich conditions, Cr vacancies are expected to dominate under synthesis environments involving  $O_2$  gas flow. This can effectively shift the Fermi level toward the lower part of the band gap. However, the  $(0/-)$  transition level of the Cr vacancy is extremely deep, suggesting that Cr vacancies are unlikely to be the source of  $p$ -type conductivity observed in some  $Cr_2O_3$  samples. [37, 38]

Experiments have observed a parasitic magnetization in Al(1.2%)-doped  $Cr_2O_3$  thin films and the parasitic magnetization can be controlled by oxygen flow condition during deposition, thereby by changing the oxygen content in the samples [39]. It was demonstrated that more oxygen lead to a larger parasitic magnetization. The spin polarized Cr vacancies – which dominates under O-rich conditions and could be easily aligned under magnetic field – could be a possible reason for this parasitic magnetization.

*c. O vacancy* The oxygen vacancy  $V_O$  in  $Cr_2O_3$  exhibits both donor and acceptor levels within the gap. Four charge-state transition levels are identified:  $(2+/+)$ ,  $(+/0)$ ,  $(0/-)$ , and  $(-2/-)$ , locating at 0.79, 1.33, 2.50, and 3.10 eV above the VBM respectively. Each charge states is associated with different local lattice relaxations. For  $V_O^{2+}$ , the four nearby Cr atoms relax outward from the vacancy by 0.15–0.21 Å. These relaxations are reduced to 0.03–0.12 Å for  $V_O^{+}$  and to 0.01–0.02 Å for  $V_O^0$ . In contrast, for the negative charge states of  $V_O$ , the nearby Cr atoms move towards the vacancy by 0.02–0.09 Å for  $V_O^{-}$  and 0.05–0.12 Å for  $V_O^{2-}$ . When Fermi level lies near mid-gap, especially between 1.33 and 2.50 eV above VBM,  $V_O$  is most likely to form in the neutral charge state. Under Cr-rich conditions, the formation energy of  $V_O^0$  is relatively low, at 1.33 eV. We further verified that  $V_O^0$  carries no spin moment and does not contribute to the global magnetization.

For a high-lying Fermi level,  $V_O$  will be in 1– or 2– charge state, depending on the position of Fermi level. We note that those negatively-charge states of  $V_O$  were missed by Ref. 13. On the other hand, Choi *et al.* reported a negative charge state of  $V_O$  in sapphire ( $Al_2O_3$ ) [40], which is iso-structural to  $Cr_2O_3$ . This is consistent with our observation.

*d. O interstitial* We investigated three possible interstitial sites for oxygen in  $Cr_2O_3$ : (i) a tetrahedral site with four neighboring Cr atoms (denoted as Tetra $_{i,4Cr}$ ), (ii) an octahedral site surrounded by six neighboring O atoms (denoted as Oct $_{i,6O}$ ) and (iii) a split interstitial configuration. These initial structures are illustrated in Fig. S4 in SM. Among these,  $O_i$  prefers the tetrahedral site with four Cr neighbors, although in the 1+ and neutral charge states it forms a split interstitial. For example, in the case of neutral  $O_i^0$ , the interstitial O displaces a nearby lattice O atom, forming an O–O dumbbell structure, as shown in Fig. S3. The O–O bond length for  $O_i^+$  and  $O_i^0$  are 1.44 and 1.42 Å, respectively. For the negatively charged state  $O_i^-$ , the local structure is similar, but

the O–O distance bond length increases to 1.91 Å. the charge-state transition levels are calculated to be 0.61 eV above the VBM for the (+/0) level, and 0.40 eV below the CBM for the (0/−) level. Compared to other intrinsic defects, the formation energy of  $O_i$  is significantly higher under Cr-rich conditions, making its incorporation unlikely. Even under O-rich conditions, where its formation energy is reduced, it remains substantially higher than that of Cr vacancies.

## 2. Defect complexes

The migration barriers of  $Cr_i$ ,  $O_i$ ,  $V_O$ ,  $V_{Cr}$  in  $Cr_2O_3$  have been previously calculated, revealing anisotropic migration behavior depending on the charge state of each defect.[13, 14] The reported migration barriers are relative modest: the lowest migration barrier for  $V_O$  is 1.22 eV, within plane migration; For  $Cr_i$ , the minimum migration barrier is 1.86 eV along [221] direction;  $V_{Cr}$  is the less mobile, with a barrier of 2.01 eV. Defect complexes involving these intrinsic defects – such as  $V_{Cr}-Cr_i$  and  $Cr_i-V_O$  – can also form. In this section, we further calculate their formation energies and binding energies to evaluate their thermodynamic stability.

The position of the Fermi level in a semiconductor with defects is governed by the condition of charge neutrality. This requires the total charge associated with all charged defects in insulating  $Cr_2O_3$  to sum to zero. Under thermodynamic equilibrium, defect concentrations are determined by their formation energies. Specifically, under Cr-rich conditions, the Cr interstitial ( $Cr_i$ ) is the dominant defect, whereas under O-rich conditions, the Cr vacancy ( $V_{Cr}$ ) prevails. Assuming that the Fermi level is pinned by  $V_{Cr}^{3-}$  and  $Cr_i^{3+}$ , the formation energies of these key native defects suggest that the Fermi level lies near midgap, around 1.8 eV. The impact of impurities on this behavior will be discussed further in Sec. III C. It is important to note that electrically active impurities can shift the Fermi level position.

*a.  $Cr_i - V_{Cr}$*  A Frenkel defect forms when an atom or ion is displaced from its lattice site and relocates to a nearby interstitial position. We investigated two configurations of Cr-associated Frenkel defect,  $Cr_i - V_{Cr}$ : one with the vacancy and interstitial aligned along the hexagonal axis (see Fig. 6b), and another with both located within the hexagonal plane. Our findings indicate that the former axial configuration is energetically favored in all charge states, by at least 2.5 eV. This defect complex exhibits multiple charge-state transition levels: (+2/+), (+/0), and (0/−), locating at 0.16, 1.15, and 2.50 eV above the VBM, respectively. When the Fermi level lies deep within the band gap, the  $Cr_i - V_{Cr}$  complex is charge neutral, with a formation energy of 2.39 eV under Cr-rich conditions. Notably, the formation energy of  $Cr_i - V_{Cr}$  under O-rich conditions is only slightly lower. To investigate the stability of the complex, we calculate its binding energy as a function of Fermi level using Eq. 5, as seen

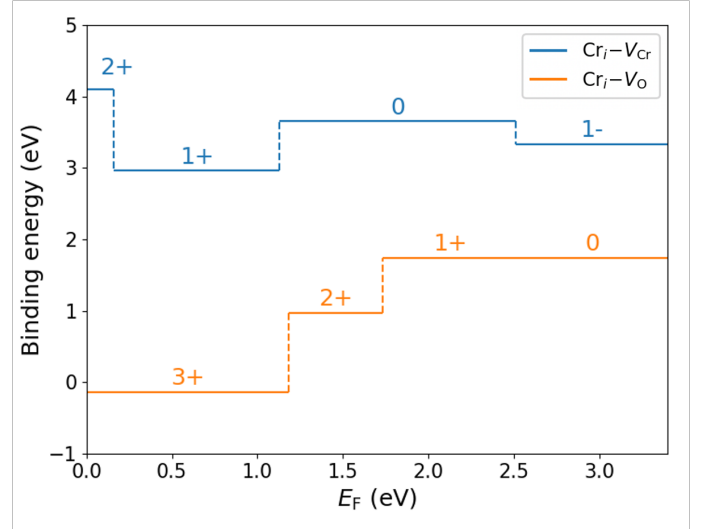


FIG. 7. Binding energy (eV) for  $Cr_i - V_{Cr}$  and  $Cr_i - V_O$  defect complex in different charge states.

from Fig. 7. This Frenkel defect is strongly bounded, a binding energy greater than 3 eV across different charge states.

*b.  $Cr_i - V_O$*  This defect complex consists of a Cr interstitial and a neighboring oxygen vacancy, as illustrated in Fig. 6(c). Three charge-state transition levels are identified within the band gap (3+/2+), (2+/+), and (+/0), located at 1.17, 1.70, and 2.52 eV above the VBM, respectively. For deep Fermi levels, the  $Cr_i - V_O$  complex is found in in neutral charge state. Under Cr-rich conditions, the formation energy of the  $Cr_i - V_O$  complex is moderately low, at approximately 2.50 eV, but it increases significantly under O-rich conditions. This indicates that the  $Cr_i - V_O$  is easier to form under Cr-rich conditions, most likely in the neutral charge state. Although the  $Cr_i - V_O$  complex is unstable in the 3+ charge state due to a negative binding energy, it becomes stable in the 2+, +, and neutral states (see the binding energy in Fig. 7). Notably, in the neutral state, the binding energy is as high as 1.74 eV.

## C. 4d and 5d transition metal defects

Using LDA+ $U$ , Ref. 12 found that isovalent Mo ( $Mo_{Cr}^0$ ) is favorable to increase the Néel temperature by 8 % per 1 % Mo doping. Here we employ hybrid functional to conduct a systematical evaluation of the 4d and 5d transition metal defects, not only to address their impact on the Néel temperature, but also investigate their capability for the defect incorporation and clarify their charge states. Six 4d and 5d transition metal elements are studied:  $X = Mo, W, Nb, Ta, Zr$  and  $Hf$ , and both interstitial ( $X_i$ ) and substitutional configurations ( $X_{Cr}$ ) are considered.

In addition, many of these defects are known to en-

hance the mechanical, thermal properties and functional properties of  $\text{Cr}_2\text{O}_3$ . For instance, Mo doping improves the passivity of  $\text{Cr}_2\text{O}_3$  [41], enhancing its corrosion resistance, while Zr doping increases hardness and provides excellent high-temperature thermal stability [42], making it attractive for protective coating applications. Understanding the formation of these dopants is therefore technologically important for optimizing such functionalities.

### 1. Substitutional defect: $X_{\text{Cr}}$

*a.  $\text{Mo}_{\text{Cr}}$  and  $\text{W}_{\text{Cr}}$*  Let's first consider the substitutional defects  $X_{\text{Cr}}$ , and we start from Mo and W dopants. There is only one type of cation site in  $\text{Cr}_2\text{O}_3$  (see Tab. I for its Wyckoff position), giving one  $X_{\text{Cr}}$ . An isolated Mo ( $4d^5 5s^1$ ) and W ( $5d^4 6s^2$ ) has six valence electrons, which is similar to Cr ( $3d^5 4s^1$ ). One may expect that both  $\text{Mo}_{\text{Cr}}$  and  $\text{W}_{\text{Cr}}$  will naturally yield isovalent cations  $\text{Mo}^{3+}$  and  $\text{W}^{3+}$  as  $\text{Cr}^{3+}$  in  $\text{Cr}_2\text{O}_3$ , i.e. +3 oxidation state. However, distinct from  $\text{Cr}_2\text{O}_3$ , Mo and W typically exhibit a +6 oxidation state, as in their stable oxide compounds  $\text{MoO}_3$  and  $\text{WO}_3$ . This indicates that  $\text{Mo}_{\text{Cr}}$  and  $\text{W}_{\text{Cr}}$  in  $\text{Cr}_2\text{O}_3$  can act as donors. This agrees with what we found from the formation energy diagram for  $\text{Mo}_{\text{Cr}}$  and  $\text{W}_{\text{Cr}}$ , as seen from Fig. 8.

For low Fermi levels in the gap, both Mo and W cations act as donors.  $\text{Mo}_{\text{Cr}}$  and  $\text{W}_{\text{Cr}}$  are in a 3+, 2+, or 1+ charge state depending on the position of Fermi level. The (1+/0) charge state transition level occurs at 1.90 and 1.27 eV below the CBM for  $\text{Mo}_{\text{Cr}}$  and  $\text{W}_{\text{Cr}}$ , respectively. Above the (1+/0) charge state transition level, both  $\text{Mo}_{\text{Cr}}$  and  $\text{W}_{\text{Cr}}$  will be in neutral charge state, i.e. isovalent to  $\text{Cr}^{3+}$ . For insulating  $\text{Cr}_2\text{O}_3$  thin film, with a  $E_F$  pinned near the mid bandgap,  $\text{Mo}_{\text{Cr}}$  will be in 0 or 1+ charge state and  $\text{W}_{\text{Cr}}$  will be in 2+ or 1+ charge state. Only when the  $E_F$  lies slightly higher than the midgap,  $\text{W}_{\text{Cr}}$  could be in neutral charge state. We will evaluate the impact of these feasible charge states on the Néel temperature of  $\text{Cr}_2\text{O}_3$  in Sec. III C 2.

The formation energy of  $X_{\text{Cr}}$  under Cr-rich conditions is notably lower than that under O-rich conditions. While this may appear counterintuitive for a substitutional dopant on the Cr site, it arises from our choice to compute the formation energies for conditions corresponding to the solubility limit, which is set by the enthalpy of formation of the limiting phase and introduces a dependence of  $\mu_X$  on  $\mu_O$ . The same trend has been reported for transition metal defects in  $\beta\text{-Ga}_2\text{O}_3$  [43]. Even under O-rich conditions, when the Fermi level locating near the mid-gap, the  $\text{Mo}_{\text{Cr}}^0$  is 3.46 eV, which is low enough to allow for the incorporation of Mo defects and the enhancement of corrosion resistance [41]. On the other hand, the formation energy of  $\text{W}_{\text{Cr}}$  is higher for high-lying Fermi level. The formation energy of  $\text{W}_{\text{Cr}}^0$  is 0.86 eV higher than that of  $\text{Mo}_{\text{Cr}}^0$  under Cr-rich conditions, indicating that the incorporation of W will be difficult.

*b.  $\text{Nb}_{\text{Cr}}$  and  $\text{Ta}_{\text{Cr}}$*  Multiples charge states of  $\text{Nb}_{\text{Cr}}$  and  $\text{Ta}_{\text{Cr}}$  (2+, 1+, 0, 1-) show up in their formation energy diagrams, as seen in the Fig. 8. The (+/0) charge-state transition levels of  $\text{Nb}_{\text{Cr}}$  and  $\text{Ta}_{\text{Cr}}$  occur at 0.74 eV and 0.45 eV below the CBM, respectively. Below the (+/0) level, Nb and Ta act a donor. When  $E_F$  lies in the mid-bandgap for insulating  $\text{Cr}_2\text{O}_3$ , both  $\text{Nb}_{\text{Cr}}$  and  $\text{Ta}_{\text{Cr}}$  will be a double donor, in +2 charge state. For high-lying  $E_F$  that is close the CBM, both  $\text{Nb}_{\text{Cr}}$  and  $\text{Ta}_{\text{Cr}}$  will act as acceptors, compensating the carriers. The (0/-) charge-state transition levels occurs at 0.22 eV and 0.09 eV below CBM for Nb and Ta, respectively.

Under O-rich conditions, the formation energies of  $\text{Nb}_{\text{Cr}}^{2+}$  and  $\text{Ta}_{\text{Cr}}^{2+}$  are 1.93 eV and 1.67 eV, respectively, when the Fermi level is pinned at the mid-gap. This is comparable to the formation energy of  $\text{Mo}_{\text{Cr}}^0$ . Similarly to Mo and W, the formation energies of  $\text{Nb}_{\text{Cr}}$  and  $\text{Ta}_{\text{Cr}}$  become much lower under Cr-rich conditions, due to the choice of solubility limit (see Sec. IIC for details). Their negative formation energies under extreme Cr-rich conditions indicate that those Nb and Ta are detrimental to the formation of bulk  $\text{Cr}_2\text{O}_3$ . Successful incorporation of these defects should be achieved under conditions closer to O-rich, rather than Cr-rich, growth environments.

*c.  $\text{Hf}_{\text{Cr}}$  and  $\text{Zr}_{\text{Cr}}$*  For a variety of  $E_F$  positions in the bandgap,  $\text{Hf}_{\text{Cr}}$  and  $\text{Zr}_{\text{Cr}}$  are single donors in 1+ charge state. (see Fig.8) This behavior contrasts with other cases where higher charge states are observed and this can be readily explained by the +4 natural oxidation state of these elements, as seen in stable oxide compounds such as  $\text{HfO}_2$  and  $\text{ZrO}_2$ . Both of  $\text{Hf}_{\text{Cr}}$  and  $\text{Zr}_{\text{Cr}}$  are relative shallow donors since their (+/0) charge-state transition levels occur 0.23 eV below the CBM.

The formation energy between  $\text{Hf}_{\text{Cr}}$  and  $\text{Zr}_{\text{Cr}}$  are pretty similar for both O-rich and Cr-rich conditions. Under O-rich conditions, Hf and Zr are easiest to incorporate due to their lowest formation energies across all the investigated transition metal defects. Assuming a Fermi energy pinning at the midgap, the formation energies of  $\text{Hf}_{\text{Cr}}^+$  and  $\text{Zr}_{\text{Cr}}^+$  are 2.09 eV and 2.22 eV, respectively. Notably, Zr incorporation is expected to enhance the mechanical properties of  $\text{Cr}_2\text{O}_3$ . [42]

### 2. Exchange energy

To investigate the impact of transition metal defects on the Néel temperature of  $\text{Cr}_2\text{O}_3$ , we use the exchange energies on the defect and on nearby Cr atoms (defined in Sec. IIB) as indicators for the Néel temperature enhancement. If the exchange energies are increased after defect incorporation, we expect an enhancement in the Néel temperature of  $\text{Cr}_2\text{O}_3$ . Since the interstitial 4d and 5d transition metals ( $X_i$ ) are difficult to be incorporated due to their high formation energies (see Sec. IIIC 3), we restrict ourselves to the discussion of the impact from substitutional defects ( $X_{\text{Cr}}$ ). Since the substitutional defects exhibit multiple charge states for different positions



TABLE II. Exchange energy on the defect site ( $E_0$ , meV) and on the first ( $E_1$ , meV) and second ( $E_2$ , meV) nearest Cr neighbors for different defect cases  $X_{Cr}^q$  in charge state  $q$ . The enhancement in Néel temperature for 1 % doping is denoted as  $\eta$  ( $\eta = \Delta T_N / T_N$ , %). The reference exchange energy in bulk  $\text{Cr}_2\text{O}_3$  is 178 meV.

	$\text{Mo}_{Cr}^0$	$\text{Mo}_{Cr}^{1+}$	$\text{W}_{Cr}^0$	$\text{W}_{Cr}^{1+}$	$\text{W}_{Cr}^{1+}$	$\text{Nb}_{Cr}^0$	$\text{Nb}_{Cr}^{1+}$	$\text{Nb}_{Cr}^{2+}$	$\text{Ta}_{Cr}^0$	$\text{Ta}_{Cr}^{1+}$	$\text{Ta}_{Cr}^{2+}$	$\text{Zr}_{Cr}^{1+}$	$\text{Hf}_{Cr}^{1+}$	$\text{Fe}_{Cr}^0$
$E_0$	755	183	970	320	108	537	238	–	–	371	–	–	–	102
$E_1$	333	109	472	101	112	136	119	122	108	107	120	129	128	164
$E_2$	279	183	346	168	221	349	305	141	307	162	144	144	145	166
$\eta$	5.8	-0.3	8.9	0.2	-0.4	4.7	2.1	0.8	0.4	0.4	-1.9	-1.8	-1.8	-0.7

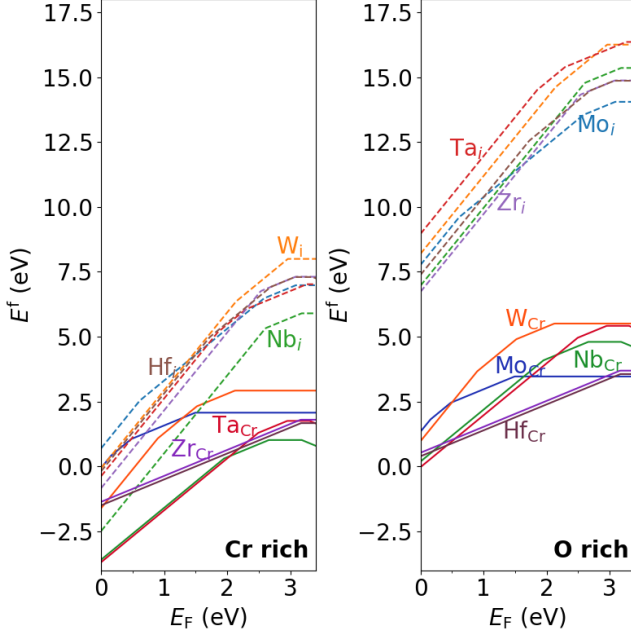


FIG. 8. Formation energy  $E^f$  of 4d and 5d transition metal defects ( $X_i$  and  $X_{Cr}$ ,  $X = \text{Mo}, \text{Nb}, \text{Zr}, \text{W}, \text{Ta}, \text{Hf}$ ) in  $\text{Cr}_2\text{O}_3$  as functions of the Fermi level  $E_F$  under (a) O-rich and (b) Cr-rich conditions.  $X_i$  represents interstitial defect, illustrated using dashed lines.  $X_{Cr}$  denotes substitution defects on Cr site, illustrated using solid lines.

of Fermi level, we confine ourselves to focus on feasible charge states when  $E_F$  locates around the midgap as in insulating samples.

Table II summarizes the exchange energies on the defect site and also on the first and second nearest Cr neighbors for various defect cases. The exchange energy on Cr in bulk  $\text{Cr}_2\text{O}_3$  is 178 meV. To benchmark our hybrid functional calculations with previous DFT+ $U$  studies [9], we calculated the exchange energy for a 3d iron impurity, and confirmed that it is detrimental to the  $T_N$  enhancement (see Tab. II). This is consistent with Ref. 9. Among the 4d and 5d impurity cases, the exchange energies on both neutral  $\text{Mo}_{Cr}^0$  and  $\text{W}_{Cr}^0$  are drastically increased to 755 meV and 970 meV, respectively. Both  $\text{Mo}_{Cr}^0$  and  $\text{W}_{Cr}^0$  defect have the  $d^3$  electron configuration, yielding a local moment of  $3 \mu_B$  (high spin). The  $d^3$  electron config-

uration corresponds to half-filled  $t_{2g}$  states, favoring *antiferromagnetic* direct exchange [33] and this is optimal for antiferromagnetic ordering. The remarkable energy enhancement for flipping the local moment of  $\text{Mo}_{Cr}^0$  and  $\text{W}_{Cr}^0$  can be understood from the electronic structure. As shown in Fig. 9, the impurity peaks for both  $\text{Mo}_{Cr}^0$  and  $\text{W}_{Cr}^0$  locate deep in the bandgap, mediating an enhanced direct exchange coupling between the spin on the defect and the spins on nearby Cr atoms. This reinforcement in the direct exchange coupling is facilitated by the reduced gap between filled (impurity)  $d$  states and empty  $d$  states for virtual electron hopping. The reason why exchange energy on  $\text{W}_{Cr}^0$  is higher than that on  $\text{Mo}_{Cr}^0$  is attributed to the fact that impurity peak of  $\text{W}_{Cr}^0$  is closer to the mid gap and its excitation gap is smaller. Additionally, the exchange energies on the Cr neighbors are increased for both  $\text{Mo}_{Cr}^0$  and  $\text{W}_{Cr}^0$ . Thanks to the in-gap impurity peaks of the  $d^3$  electron configuration! Averaging the exchange energies, we can roughly estimate the enhancement in  $T_N$  for both neutral defects: 1 % W (Mo) substitution can increase  $T_N$  by 8.9 % (5.8 %).

If the Fermi level locates at the midgap, charged defects  $\text{W}_{Cr}^{1+}$  and  $\text{Mo}_{Cr}^{1+}$  will emerge (see Fig. 8 and discussion of the charge-state transition levels in Sec. III C). We also investigate the spin energy energies for  $\text{W}_{Cr}^{1+}$  and  $\text{Mo}_{Cr}^{1+}$ , and there is no notable enhancement in the exchange energies (see Table. II). This can be explained by the  $d^2$  configuration of both charged defects, which are not optimal for antiferromagnetic interactions. This finding also suggests us to facilitate the neutral charge state of Mo and W while the 1+ charge state should be prevented. This can be achieved by adjusting the Fermi level just above the midgap to ensure their neutral charge state. From the study of intrinsic defect (Sec. III B 1), donor-like  $\text{Cr}_i$  will become dominant under Cr-rich conditions. The synthesis under Cr-rich conditions would move the Fermi level higher in the band gap, but we should also keep a substantial excitation gap (between the filled impurity peak and the empty conduction band) to prevent degrading of the device.

Turning now to  $\text{Nb}_{Cr}$  and  $\text{Ta}_{Cr}$ , Table II summarizes the exchange energies on the defect and nearby Cr atoms for 2+, 1+, and neutral charge states. The cases where the exchange energies are notably enhanced is  $\text{Nb}_{Cr}^0$  (by 4.7 % per 1 % doping) and  $\text{Nb}_{Cr}^{1+}$  (by 2.1 % per 1 % doping). As for  $\text{Nb}_{Cr}^0$ , the enhancement in the exchange

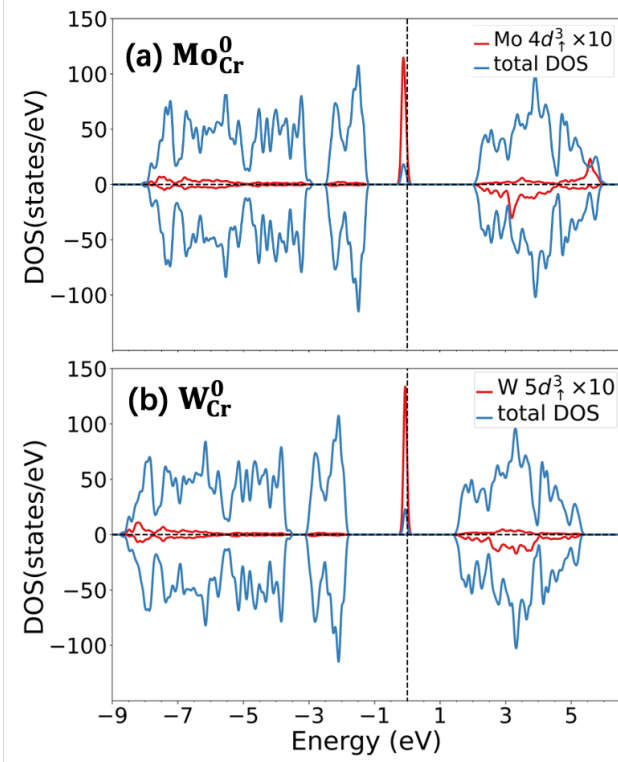


FIG. 9. (a) Total and Mo atom  $4d$  DOS for Mo substitution dope charge neutral state in  $\text{Cr}_2\text{O}_3$ . (b) Total and W atom  $5d$  DOS for W substitution dope charge neutral state in  $\text{Cr}_2\text{O}_3$ .

energy is attributed to the enhanced exchange field on the defect site and also on the next nearest Cr neighbors. The DOS of  $\text{Nb}_{\text{Cr}}^0$  [see Fig. 10 (a)] shows that the energy gap between the filled impurity levels and the unoccupied conduction bands is significantly reduced, which facilitates electron hopping. However, because the electron occupancy deviates from the optimal half-filled  $t_{2g}$  configuration, the antiferromagnetic coupling is weakened. As a result, the exchange energy is only moderately enhanced. On the other hand, while the DOS of  $\text{Ta}_{\text{Cr}}^0$  is similar to that of  $\text{Nb}_{\text{Cr}}^0$  [see Fig. 10(b)], Ta is found to be unfavorable for  $T_N$  enhancement across all investigated charge states.

The DOS of neutral Hf and Zr dopants are shown in Fig. 11. Although the ionic picture suggests one  $d$  electron on the neutral cation, our calculations reveal nearly zero local magnetic moments due to low on-site exchange. For deep Fermi levels,  $\text{Hf}_{\text{Cr}}^+$  and  $\text{Zr}_{\text{Cr}}^+$  are the relevant charge states. However, since both  $\text{Hf}_{\text{Cr}}^+$  and  $\text{Zr}_{\text{Cr}}^+$  exhibit zero local moments, they do not contribute to any exchange energy directly.

Nevertheless, the dopant-induced local relaxations can modify the nearby Cr–Cr bond lengths, thereby altering the exchange interaction parameters between neighboring Cr atoms. To assess this effect, we calculated the exchange energies on nearby Cr atoms for  $\text{Hf}_{\text{Cr}}^+$  and  $\text{Zr}_{\text{Cr}}^+$ . As shown in Table II, both dopants lead to slightly re-

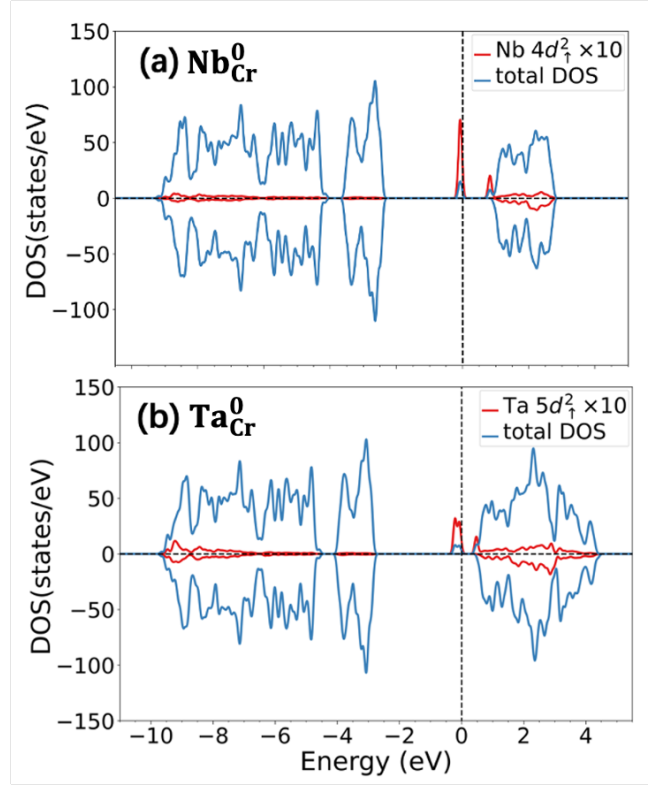


FIG. 10. (a) Total and Nb atom  $4d$  DOS for Nb substitution dope charge neutral state in  $\text{Cr}_2\text{O}_3$ . (b) Total and Ta atom  $5d$  DOS for Ta substitution dope charge neutral state in  $\text{Cr}_2\text{O}_3$ .

duced exchange energies among neighboring Cr atoms, indicating that Hf and Zr are detrimental to the  $T_N$  of  $\text{Cr}_2\text{O}_3$ .

### 3. Interstitial defect: $X_i$

As mentioned in Sec. III B 1, the inversion center (previously denoted as  $\text{Octa}_{i,60}$ ) is the most stable for Cr interstitials, and this is true for all  $4d$  and  $5d$  defects studied here. The interstitial defect  $X_i$  are easier to form under Cr-rich conditions, however, their formation energies are still substantially higher than those of substitutional defect  $X_{\text{Cr}}$  (see Fig. 8). Similar to  $\text{Cr}_i$ , multiple charge states of  $X_i$  show up, and all  $X_i$  are donors for deep Fermi level. All the charge state transition levels of  $X_i$  are summarized in SM.

Although these transition metal (TM) interstitials generally have higher formation energies compared to their substitutional counterparts, we still examine their exchange interactions. For deep Fermi levels, elements such as Ta, Zr, Hf, W, and Nb prefer the  $3+$  charge state while Mo prefers  $2+$  charge state. Interestingly, in  $\text{Zr}_i^{3+}$ ,  $\text{Hf}_i^{3+}$ , and  $\text{Nb}_i^{3+}$  cases, we observe negative exchange energies, indicating that flipping the local magnetic moment on the first nearest neighbor of the defect atom leads to a lower total energy.

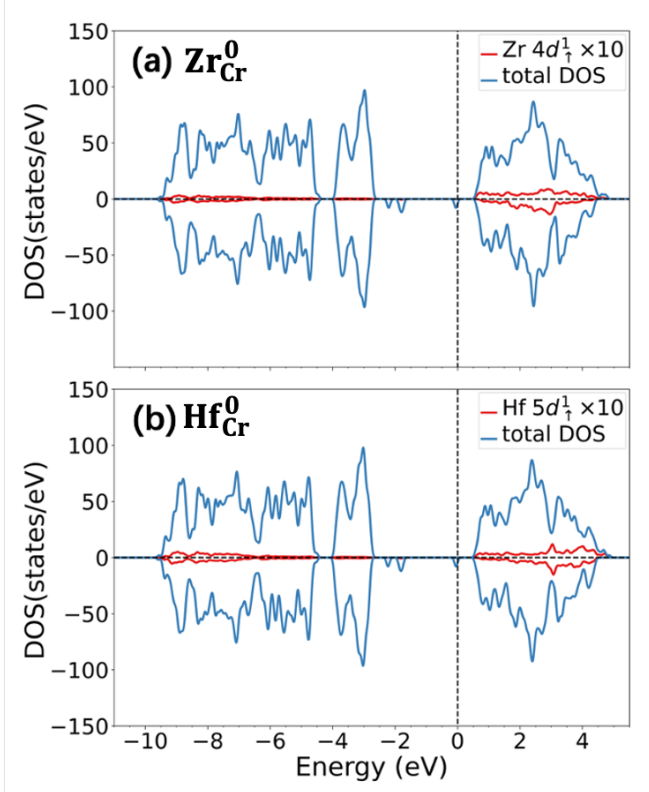


FIG. 11. (a) Total and Zr atom  $4d$  DOS for Zr substitution dope charge neutral state in  $\text{Cr}_2\text{O}_3$ . (b) Total and Hf atom  $5d$  DOS for Hf substitution dope charge neutral state in  $\text{Cr}_2\text{O}_3$ .

Additionally, we find that certain charge states of interstitial defects can significantly increase  $T_N$  of  $\text{Cr}_2\text{O}_3$  compared to their substitutional counterparts. For instance,  $\text{Hf}_i^{2+}$  leads to a 27.2 % increase of  $T_N$  per 1 % dopant, while  $\text{Ta}_i^{2+}$  doping yields a 14.1 % increase per 1 % dopant. The pronounced enhancement in the Néel temperature of  $\text{Hf}_i^{2+}$  is primarily attributed to a substantial increase in the exchange energy on second nearest neighboring (2NN) Cr atoms, from 178 and 979 meV. Moreover, an interstitial site at the inversion center is associated with six 2NNs, greatly surpassing three 2NNs as in the substitutional case, further amplifying the impact of 2NN on the Néel temperature. Further investigating the DOS of  $\text{Hf}_i^{2+}$ , we found that the substantial enhanced exchange energy on 2NN Cr atom comes from the electron redistribution of the in-gap states in two spin channels, when the 2NN Cr spin is flipped. Nevertheless, these interstitial TM defects are formidable to be incorporated due to their large formation energies, posting a great challenge to raise  $T_N$  of  $\text{Cr}_2\text{O}_3$ .

#### IV. CONCLUSIONS

In summary, we conducted a systematic first-principles study of intrinsic and extrinsic ( $4d/5d$  transition metal)

defects in  $\text{Cr}_2\text{O}_3$  to assess the likelihood of their incorporation and to identify strategies for enhancing its Néel temperature. Among the dopants examined, Mo and W substituting at the Cr site emerged as the most promising candidates. Both exhibit low formation energies under Cr-rich conditions and significantly enhance exchange interactions via impurity-mediated exchange interaction due to reduced hopping energy, particularly in their neutral charge states. Our estimates based on mean field model indicate that 1 % Mo (W) doping can raise  $T_N$  by approximately 5.8 % (8.9 %). On the other hand, substitutional Nb, Ta, Zr, and Hf defects—despite their lower formation energies—are detrimental to  $T_N$  enhancement. Additionally, interstitial transition metal defects are difficult to incorporate due to their high formation energies, despite that some of them at a certain charge state could potentially increase  $T_N$ .

We also examined intrinsic defects, their complexes, and their electrical properties. Cr interstitials ( $\text{Cr}_i$ ) and oxygen vacancies ( $\text{V}_\text{O}$ ) dominate under Cr-rich growth conditions and pin the Fermi level slightly above mid-gap, thereby stabilizing neutral Mo and W dopants, which are promising to enhance  $T_N$ . Conversely, Cr vacancies ( $\text{V}_\text{Cr}$ ) are dominant under O-rich conditions and tend to lower the Fermi level. A split Cr vacancy configuration is identified, exhibiting a slightly lower formation energy than the conventional vacancy. This split vacancy could be a possible source for the observed parasitic magnetization. A stable Frenkel pair,  $\text{Cr}_i\text{--V}_\text{Cr}$ , with a large binding energy, is found to easily form under both Cr-rich and O-rich conditions and remains charge neutral when the Fermi level lies deep within the band gap. On the other hand, the  $\text{Cr}_i\text{--V}_\text{O}$  complex is stable only in the  $2+$ ,  $1+$ , and neutral charge states, but its formation is likely only under Cr-rich conditions.

The key ingredients for enhancing the Néel temperature of  $\text{Cr}_2\text{O}_3$  via cation doping are summarized as follows:

1. Cation defects should be easily incorporated, with low or moderate formation energies.
2. The dopant should ideally exhibit half-filled electronic bands to maximize antiferromagnetic coupling.
3. For semi-insulating films with a deep Fermi level, the desired charge state corresponding to half-filling should be accessible.
4. The presence of in-gap impurity states is beneficial, as it can facilitate exchange interactions by lowering the electron hopping energy.

Our study identifies Mo and W substitutional doping under Cr-rich conditions as a promising route to enhance the magnetic performance of  $\text{Cr}_2\text{O}_3$  for spintronic applications. The detailed insights into defect energetics and magnetic interactions provide a solid theoretical foundation for future experimental optimization.

## ACKNOWLEDGMENTS

The authors acknowledge Tomohiro Nozaki for fruitful discussions and Zhi-Hao Wang for carefully reading the manuscript. This work was funded in part by an ASPIRE grant from the VPR's office at the University of South Carolina. S.M. acknowledges the startup fund from the University of South Carolina and that the Research Computing program under the Division of Information Tech-

nology at the University of South Carolina contribute to the results in this research by providing High Performance Computing resources and expertise. This work also used the Expanse supercomputer at the San Diego Supercomputer Center through allocation PHY230073 and PHY230093 from the Advanced Cyberinfrastructure Coordination Ecosystem: Services & Support (ACCESS) program, which is supported by National Science Foundation (grant numbers #2138259, #2138286, #2138307, #2137603, and #2138296).

- 
- [1] L. Landau and E. Lifshitz, *Electrodynamics of Continuous Media* (Pergamon Press, Oxford, 1960).
  - [2] C. Binek and B. Doudin, *J. Phys. Condens.* **17**, L39 (2004).
  - [3] K. D. Belashchenko, *Phys. Rev. Lett.* **105**, 147204 (2010).
  - [4] X. He, Y. Wang, N. Wu, A. N. Caruso, E. Vescovo, K. D. Belashchenko, P. A. Dowben, and C. Binek, *Nat. Mater.* **9**, 579 (2010).
  - [5] X. Chen, A. Hochstrat, P. Borisov, and W. Kleemann, *Appl. Phys. Lett.* **89** (2006).
  - [6] A. S. Borovik-Romanov and H. Grimmer, *International Tables for Crystallography*, Vol. D (Springer, Dordrecht, 2006) Chap. 1.5, pp. 105–149.
  - [7] S. Mu, *First-principles study of magnetoelectric materials*, Ph.D dissertation, University of Nebraska-Lincoln (2014).
  - [8] Y. Kota, H. Imamura, and M. Sasaki, *Appl. Phys. Express* **6**, 113007 (2013).
  - [9] S. Mu, A. L. Wysocki, and K. D. Belashchenko, *Phys. Rev. B* **87**, 054435 (2013).
  - [10] M. Street, W. Echtenkamp, T. Komesu, S. Cao, P. A. Dowben, and C. Binek, *Appl. Phys. Lett.* **104** (2014).
  - [11] A. Mahmood, W. Echtenkamp, M. Street, J.-L. Wang, S. Cao, T. Komesu, P. A. Dowben, P. Buragohain, H. Lu, A. Gruverman, *et al.*, *Nat. Commun.* **12**, 1674 (2021).
  - [12] S. Mu and K. D. Belashchenko, *Phys. Rev. Materials* **3**, 034405 (2019).
  - [13] B. Medasani, M. L. Sushko, K. M. Rosso, D. K. Schreiber, and S. M. Bruemmer, *J. Phys. Chem. C* **121**, 1817 (2017).
  - [14] B. Medasani, M. L. Sushko, K. M. Rosso, D. K. Schreiber, and S. M. Bruemmer, *J. Phys. Chem. C* **122**, 12984 (2018).
  - [15] B. K. Medasani, M. L. Sushko, K. M. Rosso, D. K. Schreiber, and S. M. Bruemmer, *J. Phys. Chem. C* **123**, 22139 (2019).
  - [16] G. Kresse and J. Furthmüller, *Phys. Rev. B* **54**, 11169 (1996).
  - [17] G. Kresse and J. Furthmüller, *Comput. Mater. Sci.* **6**, 15 (1996).
  - [18] P. E. Blöchl, *Phys. Rev. B* **50**, 17953 (1994).
  - [19] R. W. Godby, M. Schlüter, and L. J. Sham, *Phys. Rev. Lett.* **56**, 2415 (1986).
  - [20] H. J. Monkhorst and J. D. Pack, *Phys. Rev. B* **13**, 5188 (1976).
  - [21] J. Heyd, G. E. Scuseria, and M. Ernzerhof, *J. Chem. Phys.* **118**, 8207 (2003).
  - [22] D. Adler, in *Solid State Phys.*, Vol. 21 (Elsevier, 1968) pp. 1–113.
  - [23] J. A. Crawford and R. W. Vest, *J. Appl. Phys.* **35**, 2413 (1964).
  - [24] J. Zaanen, G. Sawatzky, and J. Allen, *Phys. Rev. Lett.* **55**, 418 (1985).
  - [25] C. Freysoldt, B. Grabowski, T. Hickel, J. Neugebauer, G. Kresse, A. Janotti, and C. G. Van de Walle, *Rev. Mod. Phys.* **86**, 253 (2014).
  - [26] C. G. Van de Walle and J. Neugebauer, *J. Appl. Phys.* **95**, 3851 (2004).
  - [27] H. J. Monkhorst and J. D. Pack, *Phys. Rev. B* **13**, 5188 (1976).
  - [28] C. Freysoldt, J. Neugebauer, and C. G. Van de Walle, *Phys. Rev. Lett.* **102**, 016402 (2009).
  - [29] C. Freysoldt, J. Neugebauer, and C. G. Van de Walle, *Phys. Status Solidi B* **248**, 1067 (2011).
  - [30] P. Fang and W. Brower, *Phys. Rev.* **129**, 1561 (1963).
  - [31] A. Holzheid and H. S. C. O'Neill, *Geochimica et cosmochimica acta* **59**, 475 (1995).
  - [32] G. Henkelman, B. P. Uberuaga, and H. Jónsson, *J. Chem. Phys.* **113**, 9901 (2000).
  - [33] S. Shi, A. L. Wysocki, and K. D. Belashchenko, *Phys. Rev. B* **79**, 104404 (2009).
  - [34] M. Julkarnain, J. Hossain, K. Sharif, K. Khan, *et al.*, *Can. J. Chem. Eng.* **3**, 81 (2012).
  - [35] L. W. Finger and R. M. Hazen, *J. Appl. Phys.* **51**, 5362 (1980).
  - [36] P. Brown, J. Forsyth, E. Lelièvre-Berna, and F. Tasset, *J. Condens. Matter Phys.* **14**, 1957 (2002).
  - [37] H. Cao, X. Qiu, Y. Liang, L. Zhang, M. Zhao, and Q. Zhu, *ChemPhysChem* **7**, 497 (2006).
  - [38] C.-S. Cheng, H. Gomi, and H. Sakata, *physica status solidi (a)* **155**, 417 (1996).
  - [39] T. Nozaki, M. Al-Mahdawi, Y. Shiokawa, S. P. Pati, S. Ye, Y. Kotani, K. Toyoki, T. Nakamura, M. Suzuki, S. Yonemura, *et al.*, *Phys. Status Solidi - Rapid Res. Lett.* **12**, 1800366 (2018).
  - [40] M. Choi, A. Janotti, and C. G. Van de Walle, *J. Appl. Phys.* **113** (2013).
  - [41] X. Huang, D. Costa, B. Diawara, V. Maurice, and P. Marcus, *Corros. Sci.* **224**, 111543 (2023).
  - [42] M. Mohammadtaheri, Y. Li, J. Corona-Gomez, and Q. Yang, *Surf. Coat. Technol.* **375**, 694 (2019).
  - [43] H. Peelaers and C. G. Van de Walle, *Phys. Rev. B* **94**, 195203 (2016).